UDK 691.714:629.5.017.22
Original scientific article/Izvirni znanstveni članek
ISSN 1580-2949
Mater. Tehnol.

EFFECT OF FINAL HOT-ROLLING TEMPERATURES ON THE MICROSTRUCTURE AND MECHANICAL PROPERTIES OF AN Al-CONTAINING LOW-Si TRIP STEEL

VPLIV KONČNE TEMPERATURE VALJANJA NA MIKROSTRUKTURO IN MEHANSKE LASTNOSTI TRIP JEKLA Z MAJHNO VSEBNOSTJO SILICIJA

Yingjie Yu, Bingxin Wang*
College of Mechanical Engineering, Liaoning Petrochemical University, Fushun, China

Prejem rokopisa – received: 2024-11-09; sprejem za objavo – accepted for publication: 2026-06-04

doi:10.17222/mit.2024.1340

An Al-containing low-Si TRIP steel was subjected to different final hot-rolling temperatures in the austenite non-recrystallization region during thermo-mechanical processes. The microstructural characteristics were analyzed by means of optical microscopy, transmission electron microscopy (TEM), X-ray diffraction (XRD) and electron back scattered diffraction (EBSD), and their effects on mechanical properties were investigated. The results show that lower final hot-rolling temperatures strongly promote the proeutectoid ferrite formation at the expense of bainite, which causes an increase in the amount of retained austenite (RA). Compared with higher final hot-rolling temperatures in the austenite non-recrystallization region, the steel processed at a lower temperature exhibits higher elongation and improved strength-ductility balance, due to a higher fraction of polygonal ferrite and RA particles of different sizes, which provide a sustained transformation-induced plasticity (TRIP) effect over a wide strain range. The untransformed RA in a fractured tensile specimen has a much smaller grain size and higher carbon content in comparison to the state before fracture.

Key words: Al-containing low-Si transformation-induced plasticity steel, final hot-rolling temperature, multi-phase microstructure, retained austenite, strain-hardening exponent

Avtorji v članku opisujejo termomehansko obdelavo TRIP jekla (angl.: transformation induced plasticity steel) z 1,1 % Al in majhno vsebnostjo silicija (0,52 % Si). Jeklo je bilo med termomehanskimi postopki podvrženo različnim končnim temperaturam vročega valjanja v avstenitnem območju brez rekristalizacije. Mikrostrukturne značilnosti vroče valjanega TRIP jekla so avtorji analizirali z optično mikroskopijo (OM), presevno elektronsko mikroskopijo (TEM), rentgensko difrakcijo (XRD) in difrakcijo povratno sipanih elektronov (EBSD) ter raziskali njen vpliv na mehanske lastnosti. Rezultati raziskave kažejo, da nižje končne temperature vročega valjanja močno spodbujajo nastanek proevtektoidnega ferita na račun bainita, kar povzroči povečanje količine zaostalega avstenita (RA; angl.: retained austenite). V primerjavi z višjimi končnimi temperaturami vročega valjanja v avstenitnem območju brez rekristalizacije ima jeklo predelano pri nižjih temperaturah večji raztezek in odlično kombinacijo trdnosti in duktilnosti zaradi večjih deležev poligonalnih feritnih zrn in zrn zaostalega austenita različnih velikosti, ki zagotavljajo učinek trajne transformacijsko inducirane plastičnosti (TRIP) v bistveno širšem območju deformacij. Netransformirani zaostali avstenit ima na prelomu nateznega preizkušanca veliko manjšo velikost zrn in višjo vsebnost ogljika kot jo ima preizkušanec pred izvedenim nateznim preizkusom (pred lomom oziroma plastično deformacijo).

Ključne besede: TRIP jeklo z majhno vsebnostjo silicija, končna temperatura vročega valjanja, večfazna mikrostruktura, zaostali avstenit, eksponent utrjevanja

1 INTRODUCTION

Hot-rolled TRIP steels possess not only the advantages of shorter production process and lower energy consumption, but also high elongation and outstanding strength-plasticity combination, and are widely used to fabricate structural components with higher strength in the automobile industry.[1] A typical TRIP steel microstructure is mainly comprised of polygonal ferrite along with a certain amount of bainite and small amounts of RA or martensite/austenite.[2] Under external stress, the strain-induced transformation of metastable RA to martensite enhances local strain-hardening rate, which delays the onset of necking and results in excellent elongation and combination of strength and plasticity, i. e., the TRIP effect.[3–4] Accordingly, the amount and stability of RA play a critical role in determining the mechanical properties of TRIP steels.[5,6]

RA formation is the result of carbon partitioning between austenite and ferrite (proeutectoid and bainitic ferrite).[7,8] For the hot rolling of TRIP steels, in the intercritical region of austenite+ferrite, and bainite transformation temperature range, carbon is rejected from proeutectoid ferrite and bainitic ferrite to adjacent austenite during austenite-to-ferrite transformation. Thus, with the development of austenite decomposition transformation, the residual austenite after the transformation of austenite to ferrite is gradually enriched with carbon, accompanied with an increase in the stability. Eventually,

*Corresponding author's e-mail:
bingxinwang@lnpu.edu.cn (Bingxin Wang)

residual austenite obtains a sufficiently high carbon content, and can be stabilized at room temperature, forming RA. Therefore, the formations of proeutectoid and bainitic ferrite affect the amount and stability of RA.

It is established that thermo-mechanical control processes, particularly the rolling schedules in single phase austenite region, are the keys to control austenite to ferrite transformation.[9] By changing deformation parameters, prior austenite state can be adjusted, and some structure changes are introduced in the austenite, such as refinement of the austenite grains due to recrystallization, occurrence of deformed bands and increase in the density of intragranular lattice defects in un-recrystallized austenite grains, which has a noticeable influence on the kinetics of the subsequent transformation of austenite to ferrite.[10–12]

Conventional TRIP steels usually contain a high Si content of 1–2.5 % to suppress cementite precipitation from austenite during the isothermal bainitic transformation.[13] However, during hot rolling, the high Si content produces a very stable and sticky oxide layer which is difficult to remove by pickling.[14] Similar to Si, Al is also a carbide-suppression element and helps with inhibiting cementite formation.[15] Therefore, Si can be replaced by Al in low-carbon TRIP steels.

For the sake of obtaining appropriate microstructures and desirable mechanical properties by optimizing the deformation process design, in the present work, an Al-containing low-Si TRIP steel was processed at different final hot-rolling temperatures in austenite non-recrystallization region followed by air cooling in the intercritical region of austenite+ferrite, and isothermal treatment in the bainite transformation region. The microstructural characteristics under different final hot-rolling temperatures were analyzed, as well as mechanical properties of experimental steels, in particular, strain-hardening behavior during tensile deformation, and TRIP effect were investigated. Moreover, the characteristics of RA before and after the fracture of a tensile specimen were researched.

2 METHODS AND MATERIALS

The experimental steel is a laboratory-developed Al-containing low-Si TRIP steel, and its chemical composition is shown in **Table 1**. A cast ingot with a height of 100 mm and a width of 150 mm was prepared in a 150 kg vacuum induction furnace, and forged into slabs of 60 mm in height, and 100 mm in width under 1150–1200 °C. Several critical temperatures, including the austenite non-recrystallization temperature (T_{nr}), were obtained using a Gleeble-3500 thermomechanical simulator, and listed in **Table 2**. Based on these temperature parameters, by varying the final hot-rolling temperatures in the austenite non-recrystallization region, two deformation processes, A and B, were designed, as shown in **Figure 1**. The slabs were austenitized at 1200 °C for 2 h in a resistance-heated furnace, and hot-rolled into 4.5 mm thick plates in seven passes using a pilot rolling mill with twin rolls of 450 mm in diameter. After hot rolling, the steel plates were cooled to 450 °C during a multi-step cooling process, and held for 20 min in a salt-bath furnace.

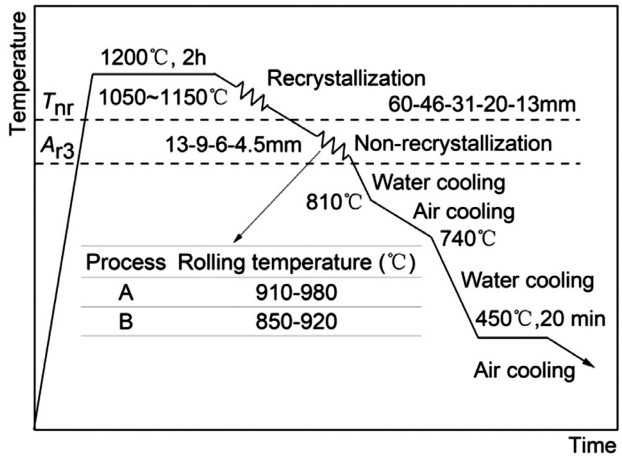

Figure 1: Schematic diagram of thermo-mechanical control process

Table 1: Chemical composition of experimental steel (*w*/%)

C	Si	Mn	Al	S	P
0.21	0.52	1.55	1.1	0.01	0.02

Table 2: Critical temperatures of experimental steel (°C)

T_{nr}	A_{r3}	A_{r1}	B_s
997	829	703	529

The specimens for microstructure observation were machined from the steel plates, and the examined planes were parallel to the rolling direction. After being mechanically polished, the samples were etched with 4 % nital solution, and observed using a Leica DMIRM image analyzer.

TEM analysis was conducted to investigate the microstructural characteristics in greater detail. Thin foils for TEM were prepared by mechanically thinning the specimens from 300 μm to 80 μm, followed by twin-jet electropolishing in an electrolyte consisting of 8 % perchloric acid and 92 % ethanol at a temperature of –30 °C. The foils were examined on an FEI Tecnai G2 F20 TEM at an accelerating voltage of 200 kv.

RA phase characteristics were analyzed using EBSD and XRD. The specimens for EBSD and XRD were obtained using mechanical polishing followed by electrochemical polishing with a solution of 80 % ethanol, 12 % distilled water and 8 % perchloric acid (volume percent) at a polishing voltage of 35 V. The specimens were examined at a 0.02 μm scan step on an FEI Quanta 600 SEM equipped with an EBSD system to evaluate the RA particle size. The carbon content and volume fraction of RA were measured using a *D*/max 2400 diffractometer equipped with a CuK_α radiation. The specimens

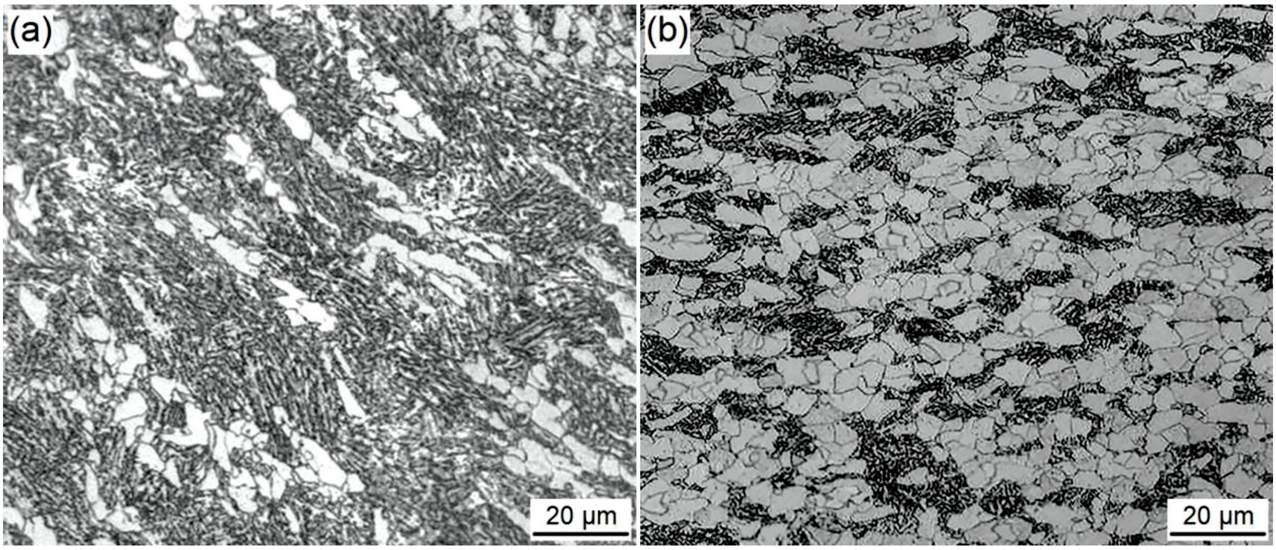

Figure 2: Microstructures of experimental steels: a) Process A, b) Process B

were scanned with a step size of 0.04° over a 2θ range of 40–130° under 55 kV and 180 mA. Integrated intensities of $(200)_\gamma$, $(220)_\gamma$ and $(311)_\gamma$ austenite peaks, and $(200)_\alpha$ along with $(211)_\alpha$ ferrite peaks were obtained by Jade version 6.5 software, and used to calculate the volume fraction of RA (V_γ) using the following equation:[17]

$$V_\gamma = \frac{1.4 I_\gamma}{I_\alpha + 1.4 I_\gamma} \tag{1}$$

where I_γ and I_α are the average integrated intensities of the above-mentioned austenite and ferrite diffraction peaks, respectively.

The carbon concentration in RA was estimated with the RA lattice parameter based on the $(220)_\gamma$ peak using the following empirical expression:[18]

$$\alpha_\gamma = 3.5467 + 0.0467 C_\gamma \tag{2}$$

Where a_γ is the lattice parameter of RA in Å, and C_γ is the carbon content of RA in *w*/%.

Rectangular tensile specimens with a gage length of 50 mm and a width of 12.5 mm were cut along the rolling direction and tested using an Instron-8500 digital control tensile testing machine. Tensile properties were determined using the average values of the test results for five tensile specimens.

3 RESULTS AND DISCUSSION

Figure 2 shows metallographic microstructures of the experimental steel subjected to different final hot-rolling temperatures. It can be seen that the volume fractions of microstructural constituents (polygonal ferrite and bainite) obtained during the two processes are

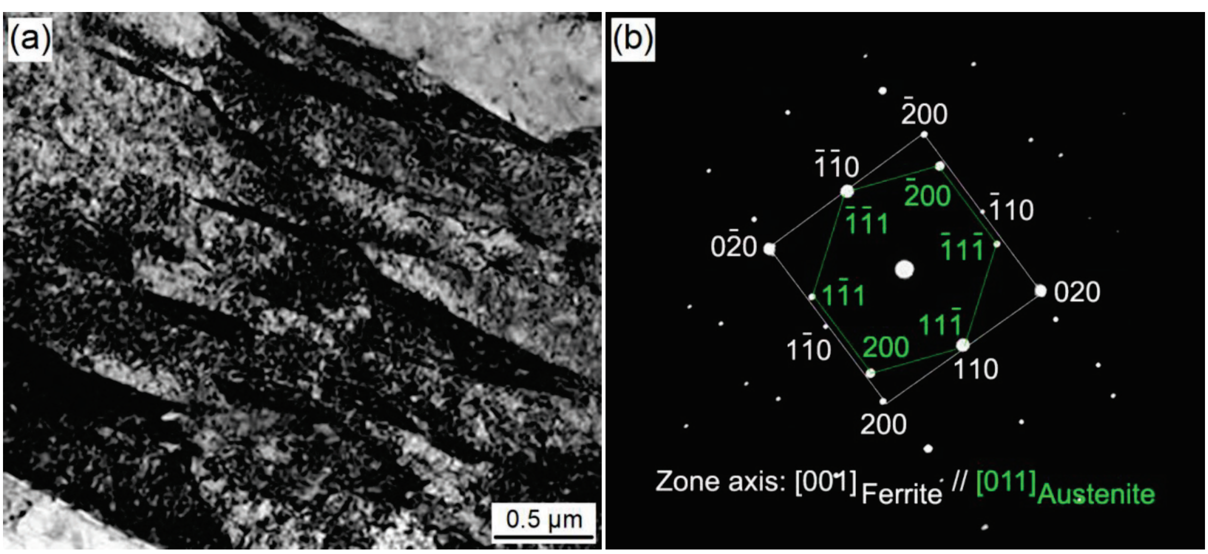

Figure 3: TEM analyses of RA after Process A: a) film-like RA distributed between bainite platelets; b) selected area electron diffraction pattern (SADP) for RA

obviously different. After Process A, the microstructure contains more bainite but less polygonal ferrite, while opposite results are observed after Process B.

RA is difficult to discern under an optical microscope. Therefore, TEM analyses of RA were performed, and the results are shown in **Figures 3** and **4**. After Process A, as indicated in **Figure 3**, RA particles are present in the form of thin interlayer films along bainitic ferrite lath boundaries. Moreover, from **Figure 3b**, it is clear that RA has the Nishiyama-Wassermann (N-W) orientation relationship of $\{110\}_{Ferrite}//\{111\}_{Austenite}$ and $\langle 100\rangle_{Ferrite}//\langle 110\rangle_{Austenite}$ with adjacent bainitic ferrite.

Similarly to Steel A, in the microstructure of Steel B, lamellar RA is also found to appear in the bainitic structure, and there is definite orientation, i.e., the Kurdjumov-Sachs (K-S) relationship of $\{011\}_{Ferrite}//\{111\}_{Austenite}$ and $\langle 111\rangle_{Ferrite}//\langle 011\rangle_{Austenite}$ between RA and the surrounding bainitic ferrite, as shown in **Figures 4a** and **4b**. However, in comparison to Steel A, RA displays some differences regarding morphology and distribution under the condition of Process B. Some blocky

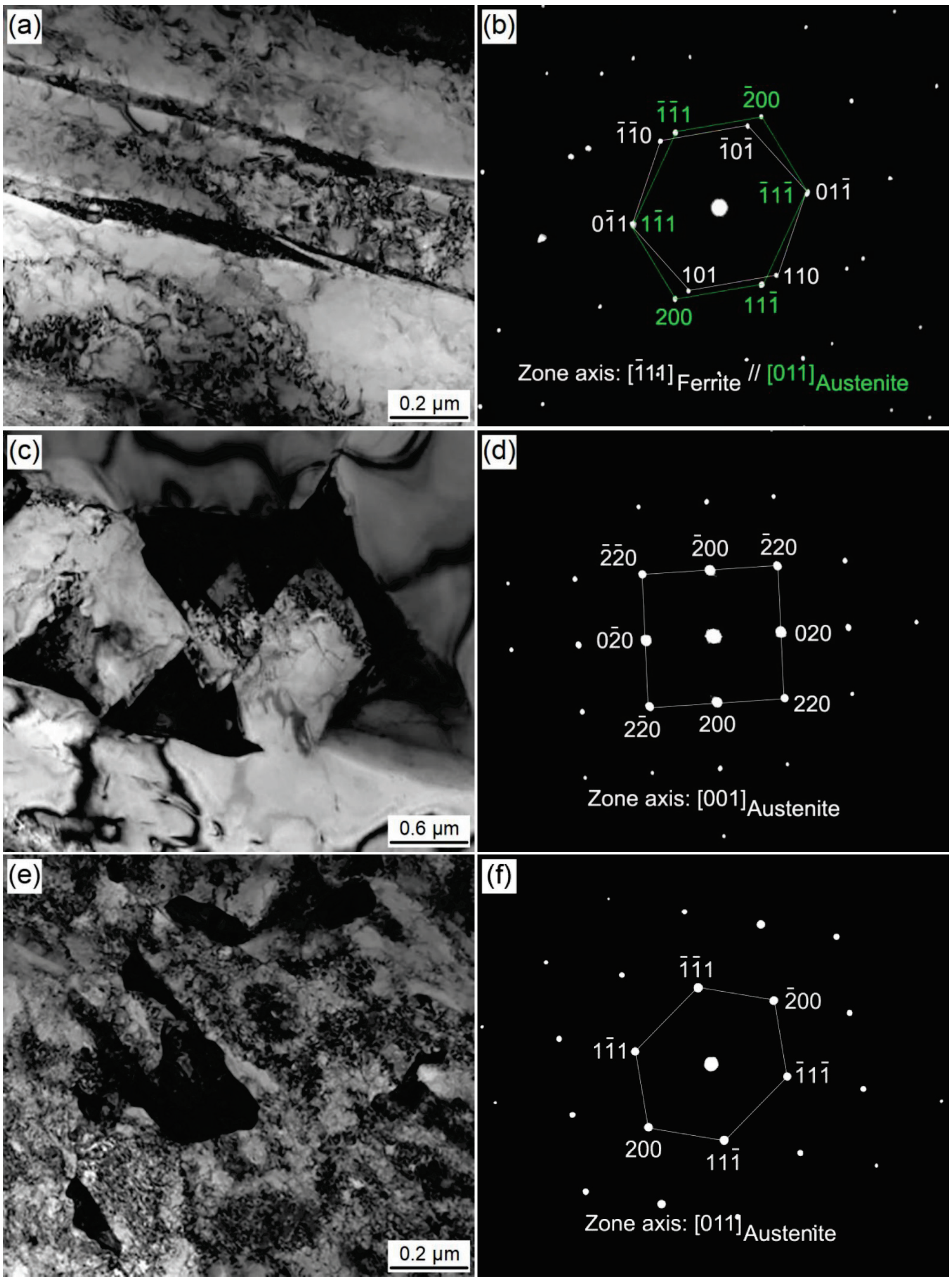

Figure 4: TEM analyses of RA for Steel B: a) lamellar RA; c) blocky RA; e) elongated and island-shaped RA; b), d) and f) SADPs for RA in a, c and e, respectively

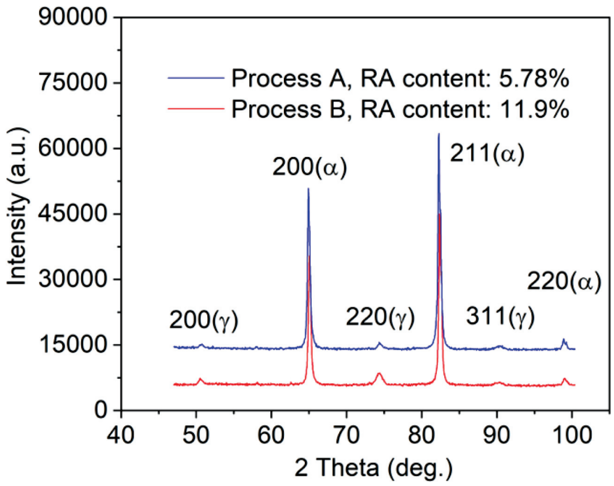

Figure 5: XRD RA data for different processes

RA particles with different sizes are trapped in polygonal ferrite grains (**Figures 4c** and **4d**), while long RA and isolated RA islands are scattered in the granular bainitic ferrite matrix (**Figures 4e** and **4f**).

Figure 5 shows XRD analysis results of RA under different final hot-rolling temperatures. Based on the XRD patterns, the volume fractions of RA are calculated to be 5.78 % for Steel A, and 11.9 % for Steel B, respectively. Obviously, the RA content of Steel B is higher than that of Steel A.

As shown above, final hot-rolling temperatures in the austenite non-recrystallization region have a remarkable effect on the metallographic microstructures, especially RA characteristics. This is mainly due to the transformation of prior austenite caused by deformation. According to the literature, deformation in the austenite non-recrystallization region can lead to strain-hardening of austenite, while lower final hot-rolling temperatures result in a more significant strain-hardening effect in prior austenite.[19]

In the strain-hardened austenite, some crystal defects caused by accumulated strain in the non-recrystallization region, such as dislocation structure and deformed bands, are formed.[10–12] Evidently, compared with higher final hot-rolling temperatures in the non-recrystallization region (i.e., Process A), the density of the lattice defects is higher in the austenite deformed at a lower temperature (Process B). After hot rolling, fast cooling (water cooling) to the given austenite+ferrite intercritical region temperature (i.e., 810 °C) can efficiently inhibit restoration behavior of strain-hardened austenite. Therefore, crystal defect structures may remain in prior austenite, usually acting as the preferred intragranular nucleation sites for proeutectoid ferrite.[10] During slow cooling in the intercritical region from 810 °C to 740 °C, in the case of Process B, a large amount of intragranular proeutectoid ferrite grains are formed due to a high density of lattice defects. Consequently, prior austenite grains are severely partitioned by intragranularly formed ferrite, resulting in a striking decrease in the particle size of remaining austenite after the intercritical region transformation. Moreover, the formation of a large amount of proeutectoid ferrite can cause noticeable carbon enrichment and a decrease in the remaining austenite surrounded by proeutectoid ferrite grains. For Process A, at the end of the intercritical region, the microstructure exhibits opposite trends in the size, amount and carbon content of the remaining austenite as well as in the amount of proeutectoid ferrite.

During holding at a temperature of 450 °C, the austenite-to-bainite transformation begins. As mentioned above, in the case of Process B, the remaining austenite exhibits a small size and low volume fraction, but a high dislocation density and high average carbon content. Carbon enrichment in austenite decreases the driving force of bainitic transformation,[19,20] and hinders the growth of bainitic ferrite via a displacive mechanism due to dislocation entanglement in austenite,[21] leading to chemical and mechanical stabilization of the remaining austenite against bainitic transformation. Moreover, the small size of the remaining austenite prior to transformation limits the development of bainitic ferrite plates due to the impingement of a large amount of intragranular ferrite. As a result, the transformation of the remaining austenite into bainite does not develop fully, which, together with the low amount of the remaining austenite, leads to a low bainitie volume fraction in the microstructure of Steel B.

Generally, carbon enrichment is more remarkable in small austenite particles during the austenite-to-ferrite transformation.[22,23] Moreover, small austenite particles exhibit high mechanical stability against bainitic and martensitic transformations, thus contributing to the austenite retention.[24] In the case of Steel B, among differently sized remaining austenite particles after the completion of proeutectoid ferrite reaction, those with a very small size are stabilized during holding at 450 °C and subsequent air cooling, becoming blocky RA distributed within the proeutectoid ferrite or at the grain boundaries of ferrite.

In contrast to Process B, the austenite-to-bainite transformation develops extensively during Process A because of lower carbon enrichment and low density of crystal-defect structures in the remaining austenite. In addition, a large amount and large particle size of remaining austenite are also the factors causing a high volume fraction of bainite, the transformation product, in the microstructure. The formation of a large amount of bainite dramatically consumes the remaining austenite accompanied with carbon enrichment in film-like residual austenite distributed between bainite platelets that can remain in the microstructure (i.e., RA). Consequently, although there is a high content of remaining austenite, the resulting volume fraction of RA is low.

The final hot-rolling temperatures in the non-recrystallization region not only cause aforementioned differences in microstructural characteristics, but also have a strong influence on the mechanical properties of the experimental steels. Therefore, the tensile properties of experimental steels were tested, and representative tensile behavior curves are given in **Figure 6**. From the stress-strain curves (**Figure 6a**), the yield strength (YS), ultimate tensile strength (UTS), total elongation (TEL), as well as the product of ultimate tensile strength and total elongation (PSE) were obtained, and listed in **Table 3**. The stress-strain (σ_e–ε_e) curves obtained from the tensile tests were converted into true stress-strain (σ–ε) ones using Equations (3) and (4).[1]

$$\sigma = \sigma_e (1+\varepsilon_e) \quad (3)$$

$$\varepsilon = \ln(1+\varepsilon_e) \quad (4)$$

Table 3: Mechanical properties of experimental steels

Processes	YS* (MPa)	UTS (MPa)	TEL (%)	UEL (%)	PSE (GPa·%)
A	528	820	24.6	17.3	20.1
B	496	760	34.1	27.2	25.9

*The yield strength (YS) is defined as the 0.2 % offset proof stress.

The Hollomon equation is usually used to describe the dependence of true stress and strain.[25] Based on the Hollomon equation, instantaneous strain-hardening exponent (n_{in}) is calculated using the relationship below,[26] and n_{in} versus ε curves are plotted, as shown in **Figure 6b**.

$$n_{in} = \frac{\varepsilon}{\sigma}\frac{d\sigma}{d\varepsilon} \quad (5)$$

The instantaneous strain-hardening exponent n_{in} reflects the uniformly strained ability. When n_{in} is equal to ε, necking is initiated.[26] Therefore, a designed $n_{in} = \varepsilon$ curve is also plotted in green dot/dash line in **Figure 6b**, and the points of intersection of the two kinds of curves are indicative of the values of the maximum uniform true strain ($\varepsilon_{umax.}$). Uniform elongation values (UEL) are calculated based on $\varepsilon_{umax.}$ data using Equation (4), and are listed in **Table 3**.

The tensile experimental results indicate that, compared with Steel A, experimental Steel B exhibits lower strength, but higher elongation (including the total elongation and uniform elongation) and product of ultimate tensile strength and total elongation. This is attributed to the differences in RA characteristics along with the volume fraction of microstructural constituents in the microstructures of the two steels. For Steel B, the TRIP effect of a large amount of differently sized RA particles remarkably improves the ductility during tensile deformation. Besides, the higher proportion of polygonal ferrite (the correspondingly lower bainite content) also enhances elongation to some extent, but decreases strength.

The contribution of the TRIP effect of RA to the ductility can be analyzed well from the strain-hardening behavior shown in **Figure 6b**. In the initial stage of deformation, n_{in} values for the two experimental steels decrease quickly to the minimum level because of dynamic restoration of soft strained ferrite.[27,28] For Steel A, the minimum n_{in} value is higher than that of Steel B because of a larger amount of bainite with high density of dislocations. After that, the two experimental steels show different strain dependence values with an increase in strain. In Steel B, the n_{in} value is gradually increased with strain, and maintained at a higher level over a considerably wide strain range before the onset of necking. On the contrary, for Steel A, the n_{in} value is lower and nearly constant over a narrower strain scope, without an increase in the n_{in} value over the entire strain range.

As mentioned above, small-sized RA particles exhibit high stability against deformation-induced transformation to martensite due to higher carbon enrichment and size effect. Moreover, the neighboring phase around RA also plays an important role in the RA stability.[29,31] The soft polygonal ferrite matrix around RA can absorb the

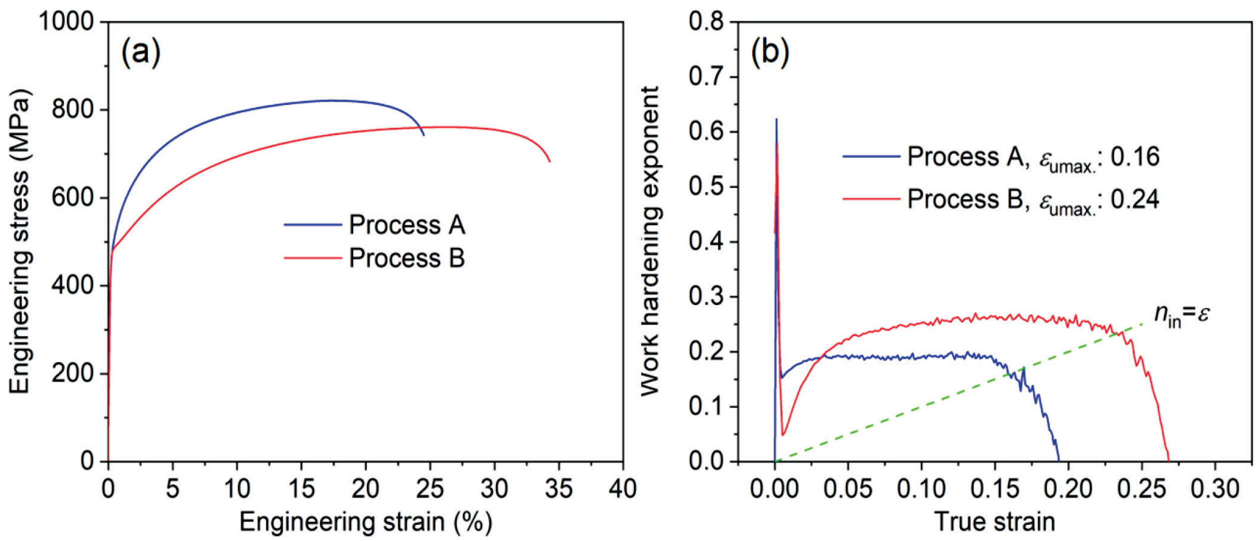

Figure 6: a) Engineering stress-strain curves and b) variation in the instantaneous strain-hardening exponent versus true strain

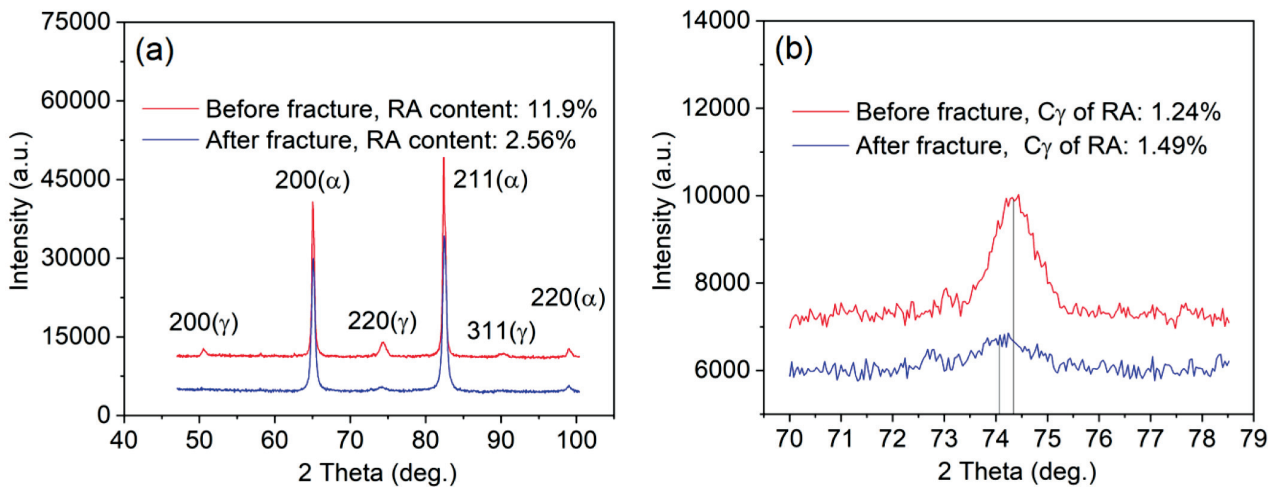

Figure 7: XRD patterns for Steel B used to calculate a) RA content and b) average carbon content in RA before and after tensile fracture

volume expansion caused by the martensite transformation, and is disadvantageous to the RA retention during strain. Conversely, bainitic ferrite can act as a shield for enclosed RA, and effectively prevent stress or strain from imposing on RA as a result of a higher yield strength, suppressing the austenite-to-martensite transformation during deformation. Therefore, film-like RA located along bainite lath boundaries and elongated RA located within granular bainitic ferrite exhibit higher stability than the RA embedded in polygonal ferrite or at ferrite boundaries, even under the same carbon content and particle size.

In Steel B, large amounts of big blocky RA with low stability easily transform into martensite in the early stage of deformation, resulting in significant strain hardening, and causing a fast and marked increase in the n_{in} value. With increasing strain, smaller blocky RA, as well as lamellar and elongated RA gradually and continuously transform into martensite owing to their higher stability, thereby maintaining a higher n_{in} value over a wide strain region. This gradual and sustained strain-hardening effect can effectively inhibit the necking initiation, and extend uniform deformation to a high strain level, producing a noticeable TRIP effect, thus dramatically improving ductility. During further straining, due to the consumption of a large amount of RA (**Figure 7**), the strain-hardening effect is weakened and accompanied with necking.

For Steel A without differently sized blocky RA, small amounts of film-like RA in the bainitic structure provide a weak and transient TRIP effect, resulting in lower elongation and poorer combination of ductility and strength compared with Steel B.

Figure 7 shows the XRD data of RA before and after tensile fracture. It can be seen from **Figure 7a** that after fracture, RA diffraction peaks have notably low intensi-

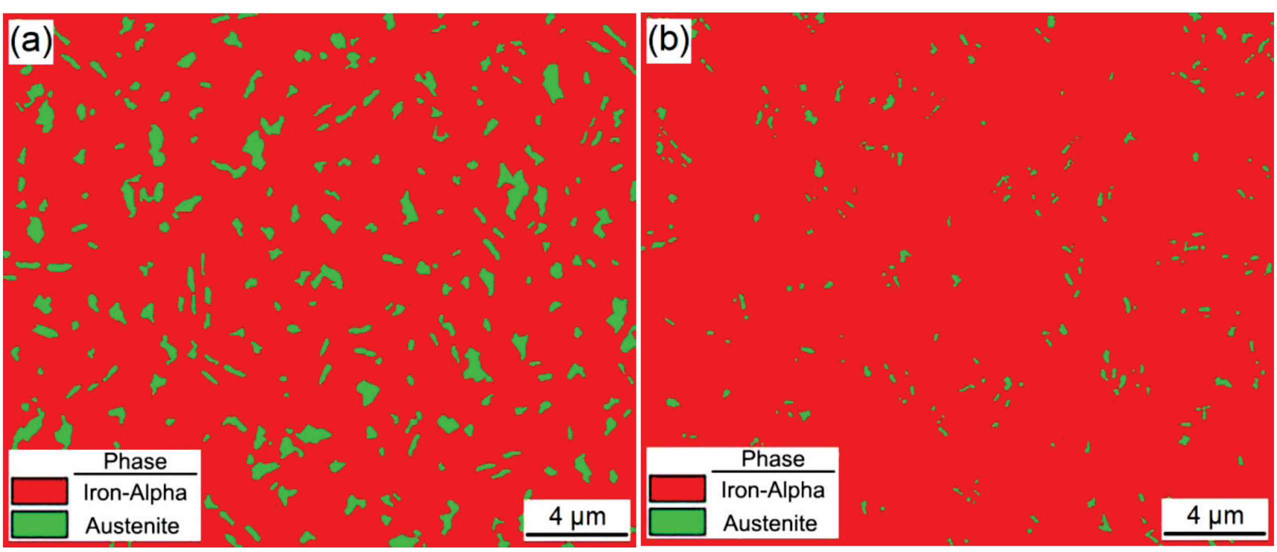

Figure 8: EBSD phase maps of Steel B before a) and after b) tensile fracture

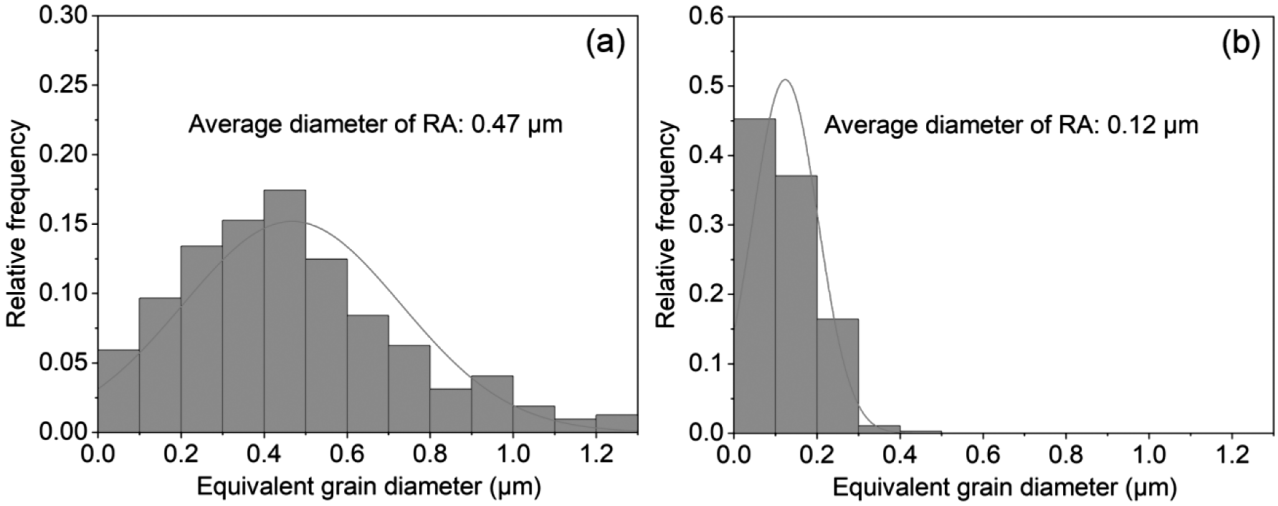

Figure 9: Distribution of the RA particle size in Steel B a) before and b) after tensile fracture

ties. Calculation results show that the content of RA after fracture decreases strikingly from 11.9 % to 2.56 %, indicating that a large amount of RA transforms into martensite during tensile deformation. Moreover, the carbon content is calculated from the $(220)_\gamma$ diffraction peak of RA shown in **Figure 7b**, indicating that the untransformed RA after fracture has a higher carbon concentration compared with that before fracture.

Figure 8 shows EBSD results for RA before and after tensile fracture, intuitively demonstrating that the RA particle size changes before and after tensile fracture. It is obvious that after fracture, the particle size of the untransformed RA becomes much smaller in comparison to that before fracture. The statistical results for the RA particle size are shown in **Figure 9**. Before fracture, the particle diameter of RA varies continually from small to large, being mainly between 0.2 μm and 0.6 μm. The RA particle average diameter is about 0.47 μm. After fracture, RA particles with diameters of more than 0.4 μm almost disappear, and particles smaller than 0.2 μm in diameter exhibit a very high frequency. The average diameter of RA particles is decreased to 0.12 μm. The above results reveal again that RA with a small particle size and high carbon content exhibits high stability.

4 CONCLUSIONS

(1) Lower final hot-rolling temperatures in the austenite non-recrystallization region strongly promote the proeutectoid ferrite formation, which causes an increase in the RA amount.

(2) Compared with higher final hot-rolling temperatures, steel deformed at lower temperatures exhibits higher elongation and an improved strength-ductility balance, due to a higher fraction of polygonal ferrite and RA particles of different sizes, which provide a sustained TRIP effect over a wide strain range.

(3) The untransformed RA in a fractured tensile specimen exhibits a much smaller grain size and higher carbon content in comparison to the state before fracture.

Acknowledgment

This work was financially supported by a Project of Education Department of Liaoning Province (grant no. LJKMZ20220743). Authors are grateful to Drs. H. Y. Wu and J. F. Wang (State Key Laboratory of Rolling & Automation of Northeastern University, China) for providing help with TEM and EBSD analyses.

5 REFERENCES

[1] A. Grajcar, A. Skowronek, K. Radwanski, Mechanical behaviour and stability of dispersed retained austenite in thermomechanically rolled and isothermally-treated TRIP-aided multiphase steel, Mater. Sci. Eng. A, 830 (**2022**), 142300, doi:10.1016/j.msea.2021.142300

[2] J. N. Huang, J. X. Yang, G. Y. Le, P. Q. Dai, H. X. Chen, J. H. Si, Z. Y. Tang, Effect of pre-quenching heat treatment time on microstructure and mechanical properties of a low-alloyed TRIP-aided steel, J. Mater. Eng. Perform., 35 (**2026**), 19509–19519, doi:10.1007/s11665-025-12962-0

[3] R. Ranjan, H. Beladi, P. D. Hodgson, S. B. Singh, The mechanical properties of low alloy TRIP-aided steel: the role of retained austenite, Metall. Mater. Trans. A, 52 (**2021**), 4649–4663, doi:10.1007/s11661-021-06417-z

[4] M. Soleimani, A. Kalhor, H. Mirzadeh, Transformation-induced plasticity (TRIP) in advanced steels: A review, Mater. Sci. Eng. A, 795 (**2020**), 140023, doi:10.1016/j.msea.2020.140023

[5] V. L. Nuam, H. Zhang, Y. C. Wang, Z. P. Xiong, Role of retained austenite in advanced high-strength steel: ductility and toughness, J. Iron Steel Res. Int., 31 (**2024**), 2079–2089, doi:10.1007/s42243-023-01165-3

[6] H. Nasr El-Din, R. Reda, Retained austenite attributes and mechanical performance of different compositions of TRIP steel alloys, J. Mater. Eng. Perform., 28 (**2019**), 2167–2177, doi:10.1007/s11665-019-04010-5

[7] J. N. Huang, Z. Y. Tang, H. Ding, R. D. K. Misra, The significant impact of phase fraction and austenite stability on the mechanical properties of a low-alloyed TRIP-aided steel: An insight into experimen-

tal analysis and predictions, Mater. Sci. Eng. A, 759 (**2019**), 40–46, doi:10.1016/j.msea.2019.05.026

[8] M. Gomez, C. I. Garcia, A. J. Deardo, The role of new ferrite on retained austenite stabilization in Al-TRIP steels, ISIJ Int., 50 (**2010**), 139–146, doi:10.2355/isijinternational.50.139

[9] Y. Onuki, T. Hirano, A. Hoshikawa, S. Sato, T. Tomida, In situ observation of bainite transformation and simultaneous carbon enrichment in austenite in low-alloyed TRIP steel using time-of-flight neutron diffraction techniques, Metall. Mater. Trans. A, 50 (**2019**), 4977–4986, doi:10.1007/s11661-019-05415-6

[10] F. Alharbi, A. A. Gazder, A. Kostryzhev, B. C. De Cooman, E. V. Pereloma, The effect of processing parameters on the microstructure and mechanical properties of low-Si transformation-induced plasticity steels, J. Mater. Sci., 49 (**2014**), 2960–2974, doi:10.1007/s10853-013-8008-z

[11] S. M. K. Hosseini, A. Zaeri-Hanzaki, S. Yue, Effect of austenite deformation in non-recrystallization region on microstructure development in low-silicon content TRIP-assisted steels, Mater. Sci. Eng. A, 618 (**2014**), 63–70, doi:10.1016/j.msea.2014.08.059

[12] Q. X. Feng, L. F. Li, W. Y. Yang, Z. Q. Sun, Microstructures and mechanical properties of hot-rolled Nb-microalloyed TRIP steels by different thermo-mechanical processes, Mater. Sci. Eng. A, 605 (**2014**), 14–21, doi:10.1016/j.msea.2014.03.051

[13] L. Y. Lan, W. Zhou, R. D. K. Misra, Effect of hot deformation parameters on flow stress and microstructure in a low carbon microalloyed steel, Mater. Sci. Eng. A, 756 (**2019**) 18–26, doi:10.1016/j.msea.2019.04.039

[14] Y. Sakuma, O. Matsumura, H. Takechi, Mechanical-properties and retained austenite in intercritically heat-treated bainite-transformed steel and their variation with Si and Mn additions, Metall. Trans. A, 22 (**1991**), 489–498, doi:10.1007/BF02656816

[15] C. Wang, H. Ding, J. Zhang, H. F. Di, Effect of partial replacement of Si with Al on the microstructures and mechanical properties of 1000 MPa TRIP steels, J. Mater. Eng. Perform., 23 (**2014**), 3896–3906, doi:10.1007/s11665-014-1190-6

[16] A. K. Srivastava, D. Bhattacharjee, G. Jha, N. Gope, S. B. Singh, Microstructural and mechanical characterization of C-Mn-Al-Si cold rolled TRIP-aided steel, Mater. Sci. Eng. A, 445–446 (**2007**), 549–557, doi:10.1016/j.msea.2006.09.101

[17] L. Liu, B. B. He, G. J. Cheng, H. W. Yen, M. X. Huang, Optimum properties of quenching and partitioning steels achieved by balancing fraction and stability of retained austenite, Scr. Mater., 150 (2018), 1–6, doi:10.1016/j.scriptamat.2018.02.035

[18] W. Cho, H. H. Lee, D. W. Suh, Effect of microstructure on mechanical properties of 1.0G TRIP steels produced by quenching and partitioning (Q&P) process, Met. Mater. Int., 31 (**2025**), 2253–2265, doi:10.1007/s12540-024-01875-7

[19] A. Zarei Hanzaki, P. D. Hodgson, S. Yue, Hot deformation characteristics of Si-Mn TRIP steels with and without Nb microalloy additions, ISIJ Int., 35 (**1995**), 324–331, doi:10.2355/isijinternational.35.324

[20] R. Ranjan, H. Beladi, S. B. Singh, P. D. Hodgson, Thermo-mechanical processing of TRIP-aided steels, Metall. Mater. Trans. A, 46 (**2015**), 3232–3247, doi:10.1007/s11661-015-2885-5

[21] T. Nakagaito, H. Matsuda, Y. Nagataki, K. Seto, Effects of partitioning of manganese and silicon during intercritical annealing on transformation behavior and mechanical properties of low alloyed TRIP-assisted steel sheets, ISIJ Int., 57 (**2017**), 380–387, doi:10.2355/isijinternational.ISIJINT-2016-288

[22] S. Lin, A. Borgenstam, A. Stark, P. Hedström, Effect of Si on bainitic transformation kinetics in steels explained by carbon partitioning, carbide formation, dislocation densities, and thermodynamic conditions, Mater. Charact., 185 (**2022**), 111774, doi:10.1016/j.matchar.2022.111774

[23] H. S. Park, J. C. Han, N. S. Lim, J.-B. Seo, C. G. Park, Nano-scale observation on the transformation behavior and mechanical stability of individual retained austenite in CMnSiAl TRIP steels, Mater. Sci. Eng. A, 627 (**2015**), 262–269, doi:10.1016/j.msea.2015.01.005

[24] G. Liu, S. G. Zhang, J. Li, J. Wang, Q. G. Meng, Fast-heating for intercritical annealing of cold-rolled quenching and partitioning steel, Mater. Sci. Eng. A, 669 (**2016**), 387–395, doi:10.1016/j.msea.2016.05.106

[25] T. Hanamura, S. Torizuka, S. Tamura, S. Enokida, H. Takechi, Effect of austenite grain size on transformation behavior, microstructure and mechanical properties of 0.1C-5Mn martensitic steel, ISIJ Int., 53 (**2013**), 2218–2225, doi:10.2355/isijinternational.53.2218

[26] A. Karimi, S. Kheirandish, M. Mahmoudiniya, Effect of bainite volume fraction on mechanical properties of a ferrite-bainite-martensite steel, Kovove Mater., 55 (**2017**), 175–182, doi:10.4149/km 2017_3_175

[27] H. Ashrafi, M. Karimi, N. Saeidi, Development of a low-carbon medium-Mn TRIP steel with an excellent combination of strength and ductility, Journal of Metals, 78 (**2026**), 3931–3939, doi:10.1007/s11837-026-08259-9

[28] D. Q. Zou, S. H. Li, J. He, Temperature and strain rate dependent deformation induced martensitic transformation and flow behavior of quenching and partitioning steels, Mater. Sci. Eng. A, 680 (**2017**), 54–63, doi:10.1016/j.msea.2016.10.083

[29] H. Rastegari, A. Kermanpur, A. Najafizadeh, Effect of initial microstructure on the work hardening behavior of plain eutectoid steel, Mater. Sci. Eng. A, 632 (**2015**), 103–109, doi:10.1016/j.msea.2015.02.040

[30] A. Lavakumar, M.-H. Park, S. Hwang, H. Adachi, M. Sato, R. K. Ray, M. Murayama, N. Tsuji, Role of surrounding phases on deformation-induced martensitic transformation of retained austenite in multi-phase TRIP steel, Mater. Sci. Eng. A, 874 (**2023**), 145089, doi:10.1016/j.msea.2023.145089

[31] X. D. Tan, H. S. He, W. J. Lu, L. Yang, B. Tang, J. Yan, Y. B. Xu, D. Wu, Effect of matrix structures on TRIP effect and mechanical properties of low-C low-Si Al-added hot-rolled TRIP steels, Mater. Sci. Eng. A, 771(**2020**), 138629, doi:10.1016/j.msea.2019.138629